# Three-dimensional flow instabilities in a thermocapillary-driven cavity

H. C. Kuhlmann* and S. Albensoeder†

*Institute of Fluid Mechanics and Heat Transfer, Vienna University of Technology, Resselgasse 3/1/2, A-1040 Vienna, Austria*

(Received 3 October 2007; published 6 March 2008)

A linear stability analysis of the buoyant-thermocapillary flow in open rectangular cavities with aspect ratios in the range $\Gamma=1.2$ to 8 is carried out for Prandtl number $\mathrm{Pr}=10$ and conditions of previous experiments. The results are in very good agreement with most available experimental data. The energy transfer between the basic and the perturbation flow reveals that buoyancy is not directly instrumental in the instabilities. For aspect ratios less than about three a stationary three-dimensional cellular flow arises. The instability relies on the lift-up mechanism operating in the shear layer below the free surface and it is aided by weak Marangoni forces. For larger aspect ratios Marangoni effects play a more significant role. While plane hydrothermal waves may appear a certain distance away from the hot wall for sufficiently large aspect ratios, the instability at intermediate aspect ratios is strongly influenced by the local nonparallel basic-flow structure.

DOI: 10.1103/PhysRevE.77.036303 PACS number(s): 47.20.Dr, 47.54.−r, 47.55.dm

## I. INTRODUCTION

Thermocapillary-driven flows are important in natural phenomena as well as in technical applications. In particular, the undesired creation of striations in crystals grown from the melt [1] has stimulated many investigations into the fundamental nature of thermocapillary flows [2]. Thermocapillary flows have been extensively studied for two fundamental finite-size geometries related to crystal growth: Cylindrical liquid bridges as models for the floating-zone technique and rectangular cavities as models for the open-boat technique. In both systems differentially heated walls drive a thermocapillary flow along the free surface. While the mechanisms causing the transition from the steady axisymmetric to the three-dimensional and eventually time-dependent flow in liquid bridges are well known, the onset of the three-dimensional flow in the rectangular system is not as fully understood. Reasons for this deficit are the change of the character of the flow as the aspect ratio varies from unity to infinity and the high numerical effort that is required to solve the stability problem in finite-size geometries: The critical Reynolds numbers in rectangular cavities are typically much higher than those in liquid bridges.

The present investigation is aimed at a numerical stability analysis of the basic two-dimensional flow in rectangular buoyant-thermocapillary cavities. In particular, we want to clarify the instability mechanisms that lead to the steady and time-dependent three-dimensional flows observed in recent experiments [3–6] using fluids with Prandtl numbers of about $\mathrm{Pr}=10$. The main factors influencing the thermocapillary cavity flow are the Prandtl number, the aspect ratios in stream- and span-wise directions, buoyancy forces, and the thermal boundary conditions.

Assuming a large or even infinite aspect ratio in span-wise direction, it is the stream-wise aspect ratio $\Gamma$ that determines the character of the flow. For aspect ratios $\Gamma$ of order unity the flow is dominated by a single vortex. If, on the other hand, the aspect ratio is very large ($\Gamma\to\infty$) the gross feature is a parallel shear flow. The instabilities of these basic steady two-dimensional flows on an increase of the driving force are thus expected to be quite different.

One of the first numerical investigations of the two-dimensional thermocapillary flow in a rectangular cavity is due to Zebib, Homsy, and Meiburg [7]. They clarified the principle flow structure in a square cavity in the absence of buoyancy, the scaling of the boundary layers, and the leading-order free-surface deformations. Their results were extended to higher Marangoni numbers by Carpenter and Homsy [8] who pointed out the analogy to the lid-driven square cavity. For $\mathrm{Pr}=1$ Carpenter and Homsy [9] considered the two-dimensional buoyant-thermocapillary flow. Keeping the ratio of buoyant to thermocapillary forces at a constant value, expressed by a constant dynamic Bond number $\mathrm{Bd}=\mathrm{Gr}/\mathrm{Re}$, the thermocapillary type of scaling was found to always dominate the buoyant one if the driving temperature difference is large enough.

On the other extreme, infinite thermocapillary layers have been investigated. The basic flow in slots has been analyzed by Sen and Davis [10] (see also [11]). The parallel flow solution far away from the end zones with zero horizontal mass flux relevant to shallow but finite cavities is called *return flow*. The seminal work on three-dimensional instabilities of infinite thermocapillary layers in the absence of gravity is due to Smith and Davis [12]. They coined the term *hydrothermal waves* for the pair of oscillatory modes which propagate under the angles of $\pm\alpha_c$ (depending on the Prandtl number) with respect to the applied temperature gradient when a critical Reynolds number is exceeded. The underlying mechanisms were elucidated by Smith [13]. An analogy between the *two-dimensional* instability in large-aspect-ratio cavities and that of the return-flow solution in infinite layers is possible for high Prandtl numbers, because the hydrothermal waves in the infinite layer are nearly two-dimensional for $\mathrm{Pr}\to\infty$ ($\alpha_c$ is small). However, the return flow in experiments can become spatially unstable prior to the onset of hydrothermal waves by virtue of the large perturbations represented by the heated walls. Depending on the Reynolds,

*h.kuhlmann@tuwien.ac.at

†Present address: CeBeNetwork GmbH, Bremen, Germany. Stefan.Albensoeder@airbus.com

 

Prandtl, and Grashof numbers a sequence of steady corotating vortices may penetrate the cavity from one of the heated walls [14,15]. Depending on the spatial stability these two-dimensional perturbations may decay or grow with the distance from the respective wall. Priede and Gerbeth [16] have carried out a more general stability analysis of the return flow solution to investigate the absolute and convective instabilities. They have shown that the return flow can become globally unstable with respect to two-dimensional corotating vortices when the buoyancy forces are sufficiently large. For $\mathrm{Pr}=13.9$ corotating vortices represent the primary instability pattern when the dynamic Bond number exceeds $\mathrm{Bd}>0.22$. Their results are in good agreement with the experimental observations of Riley and Neitzel [17] in thin layers. Corotating eddies embedded in the return flow have been found experimentally before by Villers and Platten [18] for $\mathrm{Pr}=4.24$. Mercier and Normand [19] carried out a temporal linear stability analysis for infinite thermocapillary layers, focusing on the effects of buoyancy and surface heat loss. In addition to the hydrothermal waves modified by buoyancy, they also found a steady instability which consists of convection rolls whose axes are aligned parallel to the temperature gradient.

A number of results have been obtained for intermediate aspect ratios $2 \lesssim \Gamma < \infty$. For low Prandtl numbers the results are mainly numerical. Ben Hadid and Roux [20] clarified the effect of the hot and cold wall boundaries on the steady two-dimensional flow for small Prandtl numbers. Subsequent investigations concentrated on the onset of time-dependence. Ohnishi, Azuma, and Doi [21] discovered the existence of a Hopf bifurcation in the two-dimensional thermocapillary flow for $\mathrm{Pr}=0.015$ and $\Gamma=4$. The effect of buoyancy on the two-dimensional oscillatory instability was demonstrated by Ben Hadid and Roux [22] and Mundrane and Zebib [23]. An attempt was made by the latter authors toward an analysis of the instability mechanisms by considering the energy budgets for $\mathrm{Pr}=0$ of the oscillating part of the two-dimensional solution. Schimmel, Albensoeder, and Kuhlmann [24] have carried out a linear-stability analysis of the two-dimensional thermocapillary flow in the zero-Prandtl-number limit. They established a one-to-one correspondence with the three-dimensional instabilities in the lid-driven cavity [25] in the range $\Gamma \in [0.4, 2.8]$.

The flow for higher Prandtl numbers $\mathrm{Pr}>1$ is more relevant to the present investigation. Peltier and Biringen [26] simulated the pure thermocapillary flow for $\mathrm{Pr}=6.8$ and found a two-dimensional bifurcation to oscillations for aspect ratios larger than $\Gamma \approx 2.3$. From their results one can conclude that the lateral heated boundaries have a strong stabilizing effect on the onset of two-dimensional oscillations. When the aspect ratio is increased, however, the stability boundary is reduced and approaches that of the infinite layer which was investigated by Smith and Davis [12]. Their results were confirmed and augmented by Xu and Zebib [27], who extended the analysis to three dimensions computing three-dimensional thermocapillary flows for several large aspect ratios and Prandtl numbers up to 10 (for related calculations see also [28,29]). Taking into account buoyancy Shevtsova and Legros [30] and Shevtsova, Nepomnyashchy, and Legros [31] computed the buoyant-thermocapillary flow and investigated the corotating vortices for $\mathrm{Pr}=14.8$ and $\Gamma=24.7$ as well as the transition to time dependence under the assumption that the flow remains two dimensional.

Several experimental investigation under the influence of buoyancy have been carried for Prandtl numbers $\mathrm{Pr}>1$. Saedeleer, Garcimartin, Chavepeyer, Platten, and Lebon [32] essentially confirmed the results of Ref. [18] on steady two-dimensional corotating vortices. These were also found by Riley and Neitzel [17] as well as by Schwabe *et al.* [33] for an annular geometry. Both latter investigations [17,33] were also concerned with the onset of three-dimensional time-dependent convection. The influence of different thermal boundary conditions on the high Prandtl number flow in shallow layers was considered by Ezersky *et al.* [34]. The dependence of the properties of hydrothermal waves in cavities on the global geometry, in particular on the span-wise aspect ratio, has been investigated by Pelacho *et al.* [35].

When the aspect ratio is reduced the buoyant-thermocapillary traveling-wave instability is succeeded by a steady three-dimensional instability of the steady two-dimensional flow which leads to a rectangular cellular flow pattern. One of the first reports of the three-dimensional instabilities in such a system is due to Daviaud and Vince [3] for $\mathrm{Pr}=10$. The same steady three-dimensional patterns were also found for $\mathrm{Pr}=6.78$ by Gillon and Homsy [36]. These experiments motivated two numerical-simulation runs of Mundrane and Zebib [37], who bracketed the stationary three-dimensional instability in qualitative agreement with Ref. [36]. The stationary three-dimensional patterns for $\mathrm{Pr}=10$ were also observed by other authors [4–6,38,39], confirming and/or extending the previous experiments. Similar results were also obtained by Braunsfurth and Homsy [40] for $\mathrm{Pr}=4.4$. They also found a secondary instability of the steady cellular flow to time-dependence and discussed the corresponding physical mechanism in terms of a competition of the basic (two-dimensional) thermocapillary flow and an opposing stream which is locally created by the superimposed three-dimensional cellular pattern.

It should be mentioned that some authors have also studied the related system of an annular cavity reporting similar phenomena (see, e.g., Refs. [33,41–48]). This geometry enables the elimination of the end walls in span-wise direction in favor of periodic boundary conditions at the price of a cylindrical geometry.

A satisfactory physical explanation of the observed stationary three-dimensional instability has not yet been given. The analysis is also complicated by the presence of buoyancy forces. Moreover, no linear-stability analysis has been carried out to date for the finite-aspect-ratio system. The main objective of this paper thus is to carry out a linear-stability analysis for parameters corresponding to the experiments of Refs. [3–6] and to unravel the detailed mechanisms which are governing the process of the pattern formation.

The paper is organized as follows. In Sec. II we formulate the problem, present the methods of investigation, and carry out a comprehensive code validation. The results are presented in Sec. III. We discuss the instability mechanisms in detail for the aspect ratios $\Gamma=2.1$, 4, and 8. The main findings are summarized in the conclusions.

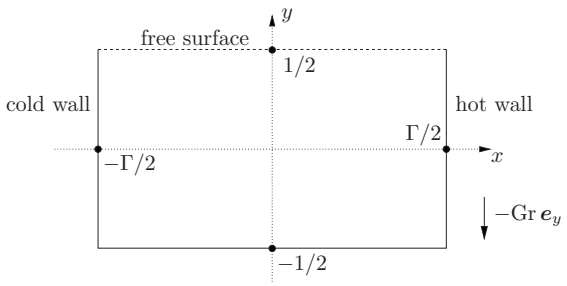


FIG. 1. Geometry of the thermocapillary-driven cavity using the height $h$ as the length scale.

## II. METHODS OF INVESTIGATION

### A. Formulation of the problem

We consider an open liquid-filled rectangular cavity of height $h$ and width $d$ in a vertical gravity field as sketched in Fig. 1. The cavity is heated from the side such that the lateral walls are maintained at a constant temperature difference $\Delta T$. The temperature difference causes a flow which is driven both by buoyancy forces and by thermocapillary stresses acting on the upper free surface.

For the numerical investigation of the flow we consider the asymptotic limit of large mean surface tension $\sigma_0$ in which the capillary number $\mathrm{Ca}=\gamma\Delta T/\sigma_0 \to 0$ vanishes, where $\gamma=-\partial\sigma/\partial T$ is the surface tension coefficient. In this limit dynamic flow-induced free-surface deformations are absent. The governing equations are further simplified by employing a Boussinesq-type approximation in which temperature variations are only taken into account in the buoyancy term and in the free-surface stress.

For the dimensionless formulation of the governing equations we use the scales $h$, $h^2/\nu$, $\nu/h$, $\rho\nu^2/h^2$, and $\Delta T$ for length, time, velocity, pressure, and temperature, respectively, where $\nu$ is the kinematic viscosity and $\rho$ the density of the liquid. If we introduce the reduced temperature $\Theta=(T-T_0)/\Delta T$, where $T_0$ is the mean temperature, the nondimensional governing equations take the form

$$\frac{\partial \mathbf{U}}{\partial t} + \mathbf{U}\cdot\boldsymbol{\nabla}\mathbf{U} = -\boldsymbol{\nabla}P + \nabla^2\mathbf{U} + \mathrm{Gr}\,\Theta\mathbf{e}_y, \tag{1a}$$

$$\boldsymbol{\nabla}\cdot\mathbf{U} = 0, \tag{1b}$$

$$\frac{\partial \Theta}{\partial t} + \mathbf{U}\cdot\boldsymbol{\nabla}\Theta = \frac{1}{\mathrm{Pr}}\nabla^2\Theta. \tag{1c}$$

Here $\mathbf{e}_y$ is the unit vector in positive $y$ direction. The dimensionless groups are the Prandtl and Grashof numbers

$$\mathrm{Pr} = \frac{\nu}{\kappa} \quad \text{and} \quad \mathrm{Gr} = \frac{g\beta\Delta T h^3}{\nu^2}, \tag{2}$$

where $\kappa$ is the thermal diffusivity, $\beta$ the thermal expansion coefficient, and $g$ the acceleration of gravity. We assume that the cavity is infinitely extended in the third ($z$) direction. The geometry is then characterized by the aspect ratio of the cross section

$$\Gamma = \frac{d}{h}. \tag{3}$$

The governing equations (1) are to be solved subject to the following boundary conditions. For the temperature field we assume perfectly conducting side walls such that the temperatures at the lateral walls can be considered fixed. The top and bottom boundaries are considered adiabatic. These assumptions lead to the thermal boundary conditions

$$\Theta\left(x = \pm\frac{\Gamma}{2}\right) = \pm\frac{1}{2} \quad \text{and} \quad \frac{\partial\Theta}{\partial y}\left(y = \pm\frac{1}{2}\right) = 0. \tag{4}$$

The velocity field must satisfy no-slip boundary conditions on both side walls and the bottom wall of the cavity. On the nondeformable free surface thermocapillary stresses must be balanced by viscous stresses. This leads to the boundary conditions for the velocity field

$$\mathbf{U}\left(x = \pm\frac{\Gamma}{2}\right) = \mathbf{U}\left(y = -\frac{1}{2}\right) = 0$$

and

$$\left[\frac{\partial \mathbf{U}_\parallel}{\partial y} + \mathrm{Re}\,\boldsymbol{\nabla}_\parallel\Theta\right]_{y=1/2} = 0, \tag{5}$$

where the velocity components and the Nabla operator tangential to the interface are defined as $\mathbf{U}_\parallel=(U,W)^{\mathrm{T}}$ and $\boldsymbol{\nabla}_\parallel=(\partial_x,\partial_z)^{\mathrm{T}}$, respectively. The strength of the thermocapillary stresses is measured by a third dimensionless group. It defines the thermocapillary Reynolds number

$$\mathrm{Re} = \frac{\gamma\Delta T h}{\rho\nu^2}. \tag{6}$$

### B. Basic state and linear stability equations

Since the system under consideration is invariant under translations in time and in $z$ direction the governing equations and boundary conditions allow for a steady two-dimensional flow. We call this state the basic flow. It is denoted by $\mathbf{u}_0(x,y)$, $p_0(x,y)$, and $\theta_0(x,y)$.

The stability of this basic flow is investigated by a linear stability analysis. To that end we decompose the total flow field

$$\begin{pmatrix}\mathbf{U}\\ P\\ \Theta\end{pmatrix} = \begin{pmatrix}\mathbf{u}_0(x,y)\\ p_0(x,y)\\ \theta_0(x,y)\end{pmatrix} + \begin{pmatrix}\mathbf{u}(x,y,z,t)\\ p(x,y,z,t)\\ \theta(x,y,z,t)\end{pmatrix}. \tag{7}$$

Inserting this ansatz into the governing equations and linearizing the equations with respect to the small perturbations $\mathbf{u}$, $p$, and $\theta$ we obtain the linear stability equations

$$\frac{\partial \mathbf{u}}{\partial t} + \mathbf{u}_0\cdot\boldsymbol{\nabla}\mathbf{u} + \mathbf{u}\cdot\boldsymbol{\nabla}\mathbf{u}_0 = -\boldsymbol{\nabla}p + \nabla^2\mathbf{u} + \mathrm{Gr}\,\theta\,\mathbf{e}_y, \tag{8a}$$

$$\boldsymbol{\nabla}\cdot\mathbf{u} = 0, \tag{8b}$$

$$\frac{\partial \theta}{\partial t} + \mathbf{u}_0 \cdot \nabla \theta + \mathbf{u} \cdot \nabla \theta_0 = \frac{1}{\mathrm{Pr}} \nabla^2 \theta. \tag{8c}$$

The boundary conditions to be satisfied by the perturbations are the same as those for the basic state, except that the temperature perturbations must vanish on the lateral boundaries, $\theta(x = \pm \Gamma/2) = 0$, because the imposed wall temperatures are already taken care of by the basic temperature field $\theta_0$.

### C. Numerical methods

The general procedure to solve the stability problem is to first calculate the basic state and then solve the linear stability problem on the same grid, using the basic state as the input. To carry out the corresponding numerical calculations the code of Albensoeder *et al.* [25] for the isothermal lid-driven cavity has been extended by adding the temperature equation and by appropriately changing the boundary conditions. Since the solution procedure is essentially the same as for the lid-driven-cavity problem, we only give a brief description of the numerical procedure. For further details the reader is referred to Ref. [25].

#### 1. Basic state

To compute the basic flow the primitive variables $(\mathbf{u}_0, p_0, \theta_0)$ are discretized on a staggered grid using finite volumes and grid stretching. The discrete nonlinear equations together with the boundary conditions can be written in compact form as

$$\mathsf{N}(\mathbf{u}_0; \mathrm{Re}, \mathrm{Pr}, \mathrm{Gr}, \Gamma) \cdot \mathbf{x} = \mathbf{b}, \tag{9}$$

where $\mathbf{x} = (\mathbf{u}_0, p_0, \theta_0)$. This system of nonlinear equations is solved using the Newton-Raphson method [49]. The solution of the linear problems which arise during the Newton-Raphson procedure is accomplished utilizing by the LAPACK program library.

To resolve the high gradients which appear near the three-phase contact lines the grid is compressed in $x$ direction toward both side walls and in $y$ direction toward the free surface. In both directions the length ratio between the largest and the smallest cell is typically 0.1. We have usually employed $141 \times 141$ grid points. If not noted otherwise, a grid with $71 \times 71$ points has been used for convergence checks. The code validation and convergence tests will be provided later in Sec. II E.

#### 2. Linear stability

Since the basic flow is uniform in $z$ direction, infinitely small deviations from it can be written as normal modes

$$\begin{pmatrix} \mathbf{u}(x,y,z,t) \\ p(x,y,z,t) \\ \theta(x,y,z,t) \end{pmatrix} = \begin{pmatrix} \tilde{\mathbf{u}}(x,y) \\ \tilde{p}(x,y) \\ \tilde{\theta}(x,y) \end{pmatrix} e^{\sigma t + \mathrm{i}(\Omega t + kz)} + \text{c.c.} \tag{10}$$

The normal mode is characterized by the wave number $k$ in $z$ direction, the oscillation frequency $\Omega$, the temporal growth rate $\sigma$, all of which are real, and the complex structure functions, indicated by a tilde, which depend on $x$ and $y$. Inserting this ansatz into the linearized equations, Eqs. (8b) and (8c), and into the corresponding boundary conditions results in a generalized eigenvalue problem of the form

$$\mathsf{A}(\mathrm{Re}, \mathrm{Pr}, \mathrm{Gr}, \Gamma, k) \cdot \hat{\mathbf{x}} = \mu \mathsf{B}(\mathrm{Pr}) \cdot \hat{\mathbf{x}}, \tag{11}$$

with the eigenvalues $\mu = \sigma + \mathrm{i}\Omega \in \mathbb{C}$ and eigenvectors $\hat{\mathbf{x}} = (\hat{\mathbf{u}}, \hat{p}, \hat{\theta}) \in \mathbb{C}$ the components of which correspond to the field variables at all grid points. Owing to the inflection symmetry $z \to -z$ of the equations the eigenvalues are either real $(\Omega = 0)$ or they arise as complex conjugate pairs $(\Omega \neq 0)$. The latter represent right and left traveling waves.

We characterize the neutral stability boundaries of the basic flow by the neutral Reynolds numbers $\mathrm{Re}_n(\mathrm{Pr}, \mathrm{Gr}, \Gamma, k)$. To determine $\mathrm{Re}_n$ the parameters Pr, Gr, $\Gamma$, and $k$ are varied such that the growth rate $\sigma = 0$ vanishes. The index $n$ indicates that for a given combination of Pr, Gr, $\Gamma$, and $k$ a set of neutral modes exists. The critical Reynolds number $\mathrm{Re}_c$ is the smallest neutral Reynolds number for a given combination of Pr, Gr, and $\Gamma$, i.e., $\mathrm{Re}_c = \min_{n,k} \mathrm{Re}_n(\mathrm{Pr}, \mathrm{Gr}, \Gamma, k)$. The associated normal mode is called the critical mode.

To solve the generalized eigenvalue problem (11) the linear-stability equations are discretized in the same way as the basic-state equations. They are then solved by inverse iteration as described in Ref. [25]. To find the critical mode for fixed parameters Re, Pr, Gr, $\Gamma$, and $k$ a sufficiently large number of eigenvalues $\mu_i$ is calculated for initial guesses $\mu_i^{(0)}$ randomly distributed in the complex plane. This is done for wave numbers dense in the interval $k \in [0;30]$. The eigenvalue with the largest growth rate is then taken as the initial guess to search for the critical point $\sigma(\mathrm{Re}) = 0$ using Newton's method.

### D. Energy budgets

For a physical understanding of the instability mechanisms an evaluation of the energy budgets of the critical modes has proven useful (see, e.g., Ref. [50]). The rate of change of the kinetic energy of the perturbation flow is given by the Reynolds-Orr equation which is written in normalized form as

$$\frac{1}{D_{\mathrm{kin}}} \frac{dE_{\mathrm{kin}}}{dt} = -1 + \sum_{i=1}^{4} \int_V I_i dV + \int_S M_1 dS + \int_S M_2 dS + \int_V B dV, \tag{12}$$

where $V = \{\mathbf{x} | \mathbf{x} \in [-\Gamma/2, \Gamma/2] \times [-1/2, 1/2] \times [0, 2\pi/k]\}$ is the volume occupied by the fluid over one wavelength $2\pi/k$ of the perturbation flow and $S = \{\mathbf{x} | \mathbf{x} \in V \text{ and } y = 1/2\}$ is the free surface over one wavelength. The integrands are

$$I_1 = -\frac{1}{D_{\mathrm{kin}}} u^2 \frac{\partial u_0}{\partial x}, \tag{13a}$$

$$I_2 = -\frac{1}{D_{\mathrm{kin}}} uv \frac{\partial u_0}{\partial y}, \tag{13b}$$

$$I_3 = -\frac{1}{D_{\mathrm{kin}}} v u \frac{\partial v_0}{\partial x}, \tag{13c}$$

$$I_4 = -\frac{1}{D_{\mathrm{kin}}} v^2 \frac{\partial v_0}{\partial y}, \tag{13d}$$

$$M_1 = \frac{1}{D_{\mathrm{kin}}} w \left.\frac{\partial w}{\partial y}\right|_{y=1/2}, \tag{13e}$$

$$M_2 = \frac{1}{D_{\mathrm{kin}}} u \left.\frac{\partial u}{\partial y}\right|_{y=1/2}, \tag{13f}$$

$$B = \frac{\mathrm{Gr}}{D_{\mathrm{kin}}} v \theta. \tag{13g}$$

All terms have been normalized by the rate of energy dissipation which, for the present boundary conditions, can be written as

$$D_{\mathrm{kin}} = \int_V \boldsymbol{\omega}^2 dV, \tag{14}$$

where $\boldsymbol{\omega} = \boldsymbol{\nabla} \times \mathbf{u}$ is the vorticity of the perturbation flow. The terms $I_i$ represent convective energy-transfer processes, $M_i$ indicates the work per time and surface area done by Marangoni forces, and $B$ is the work per time and volume carried out by the buoyancy forces.

In a similar way the transfer of thermal energy can be specified. Note, however, that the thermal energy density, defined as $\theta^2/2$, is just a positive measure for the perturbation-temperature field and has nothing to do with the thermal energy in the thermodynamic sense. The thermal energy balance is obtained by multiplying the temperature equation (8c) by $\theta$ and integration over the volume. We obtain

$$\frac{\mathrm{Pr}}{D_{\mathrm{th}}} \frac{d}{dt} E_{\mathrm{th}} = -1 + \sum_{i=1}^{2} \int_V J_i \, dV, \tag{15}$$

where the integrands

$$J_1 = -\frac{\mathrm{Pr}}{D_{\mathrm{th}}} \theta u \frac{\partial \theta_0}{\partial x}, \tag{16a}$$

$$J_2 = -\frac{\mathrm{Pr}}{D_{\mathrm{th}}} \theta v \frac{\partial \theta_0}{\partial y} \tag{16b}$$

describe the production of thermal energy by convective transport of the basic-state temperature field caused by the perturbation flow. All terms have been normalized by the thermal dissipation term

$$D_{\mathrm{th}} = \frac{1}{\mathrm{Pr}} \int_V (\boldsymbol{\nabla} \theta)^2 dV. \tag{17}$$

### E. Code validation

The isothermal code has been validated extensively both regarding the two-dimensional basic flow [51] as well as regarding the linear stability analysis [25,50,52]. Additional validations have been carried out for the present nonisothermal flow.

As a first step the computed two-dimensional steady flow is validated for different parameter combination. Since we always consider $\mathrm{Re} \neq 0$ we shall use the dynamic Bond number $\mathrm{Bd} = \mathrm{Gr}/\mathrm{Re} = \rho g \beta h^2 / \gamma$ to characterize the gravity level. This parameter has the advantage of immediately giving the importance of buoyancy relative to thermocapillarity. The comparison with data previously published by Refs. [8,9,26,27] is made in Table I. Our calculations are in good agreement with the data from the literature, except for the parameter set ($\mathrm{Pr} = 30$, $\mathrm{Re} = 2 \times 10^3$). This case represents the highest Marangoni number considered, $\mathrm{Ma} = \mathrm{Re}\,\mathrm{Pr} = 6 \times 10^4$. All previous computations show a significant deviation from the present converged data, particularly for the vortex strength as expressed by the maximum stream function $\psi_{\mathrm{max}}$ or the vorticity $\omega_c$ in the center of the vortex. Since our results agree with the previous references for all other (moderate) Marangoni numbers and because we have clearly obtained grid convergence for the high-Marangoni-number case we attribute the deviations for $\mathrm{Ma} = 6 \times 10^4$ to an insufficient resolution of the older investigations.

The linear stability analysis is validated for several cases. The first test case considered is a side-heated purely buoyancy-driven cavity in which the free surface is replaced by a rigid lid. In case of perfectly conducting boundary conditions at the top and bottom walls the horizontal temperature profiles along these walls are identical and linear. For adiabatic top and bottom walls the boundary condition $\partial_y \Theta = 0$ was imposed on these walls. Henkes and Le Quéré [53] calculated the linear stability for a cavity with a square cross section filled with a fluid of $\mathrm{Pr} = 0.71$. In the conducting case they found a steady three-dimensional critical mode. The critical Rayleigh and wave numbers $\mathrm{Ra} = \mathrm{Gr}\,\mathrm{Pr}$ and $k_c$ were bracketed to $\mathrm{Ra}_c \in ]10^6; 1.8 \times 10^6[$ and $k_c \in ]5.7; 10.5[$, respectively. In our present calculations we find the critical Rayleigh number $\mathrm{Ra}_c = (1.273 \pm 0.050) \times 10^6$ and the critical wave number $k_c = 5.835 \pm 0.023$. Both values match with the intervals given by Ref. [53]. For the adiabatic case Ref. [53] found a steady three-dimensional mode as well which becomes supercritical for $\mathrm{Ra}_c \in ]10^7; 10^8[$ with $k_c \in ]7.8; 62.8[$. In our calculations we find the critical parameters $\mathrm{Ra}_c = (15.47 \pm 0.11) \times 10^6$ and $k_c = 19.160 \pm 0.095$. Again both critical parameters fit the given intervals of Ref. [53]. For both types of boundary conditions the structure of the critical modes that we have calculated is qualitatively the same as the small-amplitude modes computed by Henkes and Le Quéré [53] and shown in their figures.

As another test case, we compare our linear stability result with the three-dimensional open-cavity flow simulated numerically by Mundrane and Zebib [37] for $\mathrm{Pr} = 8.4$, $\mathrm{Bd} = 5.76$, and $\Gamma = 1.47$. They used the span-wise aspect ratio $\Lambda = 1.4$ and employed free-slip boundary condition at $z = \pm \Lambda/2$. These conditions represent restricted periodic boundary conditions which are compatible with periodic flows for which the span-wise velocity component $w$ vanishes exactly on the boundaries at $z = \pm \Lambda/2$, but which are not generally compatible with span-wise traveling waves. For large simulation times one of their two simulations con-

TABLE I. A comparison of typical basic-state data with previously published results for three different cases. The Nusselt number is defined as $\mathrm{Nu}=-\int_{-1/2}^{1/2}(\partial\theta_0/\partial x)dy$.

| Grid/Author | max $\psi$ | $\omega_c$ | $x_c$ | $y_c$ | $u(0,0.5)$ | $\mathrm{Nu}_{x=-0.5}$ | $\mathrm{Nu}_{x=0}$ | $\mathrm{Nu}_{x=0.5}$ | $\max_{x_m} u\|_{y=0.5}$ | $x_m$ |
|---|---|---|---|---|---|---|---|---|---|---|
| | | | | | Re=10000, Pr=1, $\Gamma$=1, Bd=0 | | | | | |
| Carpenter and Homsy [8] | 32.3 | 697 | −0.08 | 0.12 | −296 | 4.33 | 4.40 | 4.36 | — | — |
| Xu and Zebib [27] | 32.1 | 701 | −0.07 | 0.13 | −305 | 4.36 | — | 4.36 | — | — |
| Peltier and Biringen [26] | 32.4 | 729 | — | — | −306 | 4.44 | 4.36 | 4.30 | — | — |
| 71×71 | 32.177 | 704.97 | −0.068 | 0.119 | −304.55 | 4.365 | 4.356 | 4.365 | −887.10 | −0.496 |
| 115×115 | 32.192 | 697.58 | −0.083 | 0.133 | −304.36 | 4.364 | 4.357 | 4.364 | −752.35 | −0.495 |
| 141×141 | 32.213 | 703.41 | −0.068 | 0.128 | −304.32 | 4.364 | 4.359 | 4.364 | −741.35 | −0.496 |
| 211×211 | 32.215 | 702.35 | −0.068 | 0.131 | −304.27 | 4.363 | 4.361 | 4.363 | −711.87 | −0.496 |
| | | | | | Re=2000, Pr=30, $\Gamma$=1, Bd=0 | | | | | |
| Carpenter and Homsy [8] | 4.26 | 148 | — | — | −37.2 | 6.60 | 6.29 | 6.42 | — | — |
| Xu and Zebib [27] | 3.38 | 125.4 | −0.07 | 0.28 | −29.8 | 6.61 | — | 6.61 | — | — |
| Peltier and Biringen [26] | 3.64 | 130.6 | — | — | −32.2 | 6.69 | 6.71 | 7.14 | — | — |
| 71×71 | 2.9392 | 108.90 | 0.099 | 0.276 | −24.681 | 6.303 | 6.271 | 6.303 | −169.69 | −0.496 |
| 115×115 | 2.8932 | 113.35 | 0.101 | 0.287 | −24.223 | 6.262 | 6.250 | 6.262 | −199.85 | −0.498 |
| 141×141 | 2.8825 | 111.14 | 0.099 | 0.284 | −24.116 | 6.250 | 6.242 | 6.250 | −210.64 | −0.498 |
| 211×211 | 2.8683 | 109.03 | 0.099 | 0.281 | −23.982 | 6.234 | 6.230 | 6.234 | −225.05 | −0.499 |
| | | | | | Re=5000, Pr=1, $\Gamma$=1, Bd=10 | | | | | |
| Carpenter and Homsy [9] | 16.45 | 248.5 | — | — | −179 | 4.17 | 4.15 | 4.14 | — | — |
| 71×71 | 16.296 | 244.36 | −0.155 | 0.160 | −175.73 | 4.548 | 4.545 | 4.548 | −451.29 | −0.492 |
| 115×115 | 16.338 | 240.79 | −0.153 | 0.158 | −175.90 | 4.546 | 4.545 | 4.546 | −431.57 | −0.493 |
| 141×141 | 16.345 | 244.85 | −0.155 | 0.159 | −175.93 | 4.546 | 4.545 | 4.546 | −425.58 | −0.492 |
| 211×211 | 16.356 | 230.55 | −0.147 | 0.151 | −175.97 | 4.545 | 4.545 | 4.545 | −420.41 | −0.492 |

verged to a steady two-dimensional flow while the other one, for a higher Marangoni number, yielded a steady three-dimensional flow. It was concluded that a three-dimensional flow instability must occur for some Marangoni number within the rather wide range $\mathrm{Ma}_c \in ]2.93\times10^3; 1.95\times10^5[$. For a comparison we carried out a linear stability analysis for $k_c$=4.488, i.e., for normal modes whose wavelength corresponds to the span-wise aspect ratio $\lambda=\Gamma=1.4$. Using this wave number our linear stability analysis yielded a steady critical mode which is, in fact, compatible to the free-slip conditions used by Ref. [37]. Moreover, we obtained a critical Marangoni number of $\mathrm{Ma}_c=64\,660\pm765$($k$=4.488), which is consistent with the previous simulations of Ref. [37]. As for the previous comparison, the critical mode of our linear stability analysis is found to be very similar to the three-dimensional flow structure computed by Mundrane and Zebib [37].

We also compared our results with the calculations of Xu and Zebib [27] who simulated the flow in open rectangular thermocapillary-driven cavities in the absence of gravity (Bd=0). The end walls in $z$ direction at $z=\pm\Lambda/2$ were modeled by no-slip adiabatic boundaries. Reference [27] studied the flow for the Prandtl-number and aspect-ratio combinations $(\mathrm{Pr},\Gamma,\Lambda)=(4.4,3,20)$, (13.9,3,20), and (13.9,15,15). The rather large values of $\Lambda$ were intended to approximate an infinite system in span-wise direction, as is considered in the present linear stability analysis. In Table II we compare our critical data for two- and three-dimensional instabilities with those given by Ref. [27]. For $(\mathrm{Pr},\Gamma)=(4.4,3)$ and $(\mathrm{Pr},\Gamma)=(13.9,15)$ a good to satisfactory agreement is achieved. However, for the case $(\mathrm{Pr},\Gamma)=(13.9,3)$ the parameters differ substantially for both two- and three-dimensional instabilities. To clarify this discrepancy we recalculated the stability curves $\mathrm{Re}_c(\Gamma)$ for Pr=4.4, Pr=6.78, and Pr=10 as shown in Figs. 1 and 2 of Ref. [27]. We find a good agreement between their and our results, except for the the case $(\mathrm{Pr},\Gamma)=(13.9,3)$. Since our results can be considered grid converged (see below), we conclude that the results of Xu and Zebib [27] for $(\mathrm{Pr},\Gamma)=(13.9,3)$ must be considered with care.

Finally, our linear-stability results for large aspect ratios can be compared with the linear-stability analysis of the return flow in an infinite horizontal thermocapillary layer [12], as was also done by Ref. [27]. Since the results of Smith and Davis [12] lack some accuracy for extreme Prandtl numbers (for $\mathrm{Pr}\to0$ and $\mathrm{Pr}\to\infty$), we use the corrected data provided by Ref. [2]. For the large aspect ratio $\Gamma$=15 and Pr=13.9 the surface temperature varies strongly near the heated walls owing to the thermal boundary layers on these walls. A comparison with the infinite layer is possible, because the surface temperature varies nearly linearly over the remaining wide and central area of the free surface. At the critical onset for

TABLE II. Critical parameters for two- (a) and three-dimensional instabilities (b) obtained by the linear stability analysis ($\Lambda \to \infty$) in comparison with the results of Xu and Zebib [27]. Values for $k_c$ of Ref. [27] have been graphically deduced from their graphs. The numerical resolution for the linear stability analysis is $241 \times 90$ for $\Gamma = 15$. The specified error bounds are based on comparisons with data obtained on grids half as fine, i.e., $121 \times 45$.

(a) Two-dimensional instability

| Author | $\Gamma$ | Pr | $\mathrm{Re}_c^{2D}$ | $\Omega_c$ |
|---|---|---|---|---|
| Present | 3 | 4.4 | $2026.6 \pm 2.8$ | $16.537 \pm 0.006$ |
| Xu and Zebib | 3 | 4.4 | 1950 | 11.4 |
| Present | 3 | 13.9 | $1197.7 \pm 5.4$ | $11.076 \pm 0.003$ |
| Xu and Zebib | 3 | 13.9 | 770 | |

(b) Three-dimensional instability

| Author | $\Gamma$ | $\Lambda$ | Pr | $\mathrm{Re}_c^{3D}$ | $k_c$ | $\Omega_c$ |
|---|---|---|---|---|---|---|
| Present | 3 | $\infty$ | 4.4 | $844.9 \pm 3.3$ | $1.618 \pm 0.010$ | $8.010 \pm 0.002$ |
| Xu and Zebib | 3 | 20 | 4.4 | 850 | $\approx 1.57$ | — |
| Present | 3 | $\infty$ | 13.9 | $861 \pm 65$ | $0.957 \pm 0.004$ | $3.451 \pm 0.057$ |
| Xu and Zebib | 3 | 20 | 13.9 | 1000 | — | — |
| Present | 15 | $\infty$ | 13.9 | $690.7 \pm 11.3$ | $1.049 \pm 0.023$ | $3.456 \pm 0.088$ |
| Xu and Zebib | 15 | 15 | 13.9 | 700 | $\approx 1.26$ | $\approx 3.14$ |

hydrothermal waves we find a free-surface temperature gradient $\partial\theta_0/\partial x|_{y=1/2} = 0.0313$. If we denote values deduced from the bulk exclusive of the boundary regions near the heated walls with an asterisk, the associated critical parameters are $\mathrm{Ma}_c^* = \mathrm{Re}_c \,\mathrm{Pr}\, \partial\theta/\partial x|_{y=1/2} = 300.5$, $k_c^* = (k_c^2 + \beta_c^2)^{1/2} \approx 2.80$, and $\Omega_c^*/k_c^* \,\mathrm{Re}_c^* \approx 0.057$, where $\beta_c$ is the approximated critical wave number in $x$ direction. These critical data compare very well with the results for the infinite layer $\mathrm{Ma}_c^* \approx 290$, $k_c^* \approx 2.53$, and $\Omega_c^*/k_c^* \,\mathrm{Re}_c^* = 0.0606$ [2]. Also, away from the heated walls the angle with respect to the $x$ axis at which the waves propagate is found to be $\alpha_c^* \approx \pm 22.0$. This is consistent with the angle $\alpha_c^*(\mathrm{Pr}=13.9) \approx \pm 17°$ which the hydrothermal waves in the infinite layer make with the direction of the surface-temperature gradient [2]. Xu and Zebib [27] obtained $\alpha_c^* \approx \pm 15$.

In the previous validations most critical parameters were specified up to an error estimate. This error estimate is based on the difference which the respective quantity on the actual fine grid makes with the same quantity on a grid which is half as fine. From the relatively small errors we conclude that a good grid convergence is obtained. To demonstrate the grid convergence in more detail the critical Reynolds numbers for the buoyant-thermocapillary flow are plotted in Fig. 2 as functions of the inverse of the number of grid points for several aspect ratios $\Gamma$. In all cases considered the critical Reynolds number is nearly a linear function of $1/N^2$, i.e., the convergence is quadratic. The relative difference between $\mathrm{Re}_c(N=141)$ and $\mathrm{Re}_c(N=71)$ is less than 4% throughout. Actually, it is much better in most cases. To summarize, the present linear stability results are in good agreement with the literature data, except for a single case. Moreover, second-order convergence is achieved.

## III. RESULTS

Since the parameter space of the problem is large, we shall confine ourselves to data for which experimental results are available. In particular, we aim at a better understanding of the pattern formation which has been observed in a thermocapillary cavity by Daviaud and Vince [3] for $\mathrm{Pr}=10$ and $\Gamma^2\,\mathrm{Bd}=12.755$. In fact, these parameters are within the range of values for which we have shown our numerics to be convergent and valid.

### A. Stability boundary

We consider the buoyant-thermocapillary cavity flow for $\mathrm{Pr}=10$ and $\Gamma^2\,\mathrm{Bd}=12.755$. These parameters correspond to the material and geometry parameters of the experiment of Daviaud and Vince [3]. Also Sakurai *et al.* [4,5] and Burguete *et al.* [6] performed experiments for similar parameters (Table III). The working fluid in all experiments listed in the table was silicone oil with nominal kinematic viscosity of $\nu \approx 0.65$ cSt. The capillary number can be estimated as $\mathrm{Ca} \approx 5 \times 10^{-3} \Delta T/\mathrm{K}$ [6]. With an expected critical temperature difference of $\Delta T_c = O(4\ \mathrm{K})$ the capillary number at the onset is about $\mathrm{Ca}(\Delta T_c) \approx 2 \times 10^{-2}$ or larger. This estimate justifies our numerical model which assumes a flat and nondeformable surface corresponding to the limit $\mathrm{Ca} \to 0$, at least for a certain range of critical and supercritical conditions.

In all three sets of experiments mentioned above two types of instabilities were observed: for small aspect ratios $\Gamma$ the supercritical three-dimensional flow was found to be steady, whereas it turned out to be oscillatory for larger aspect ratios. The results of our linear stability analyses are shown in Figs. 3 and 4 together with available experimental data. To provide quantitative information we have also listed

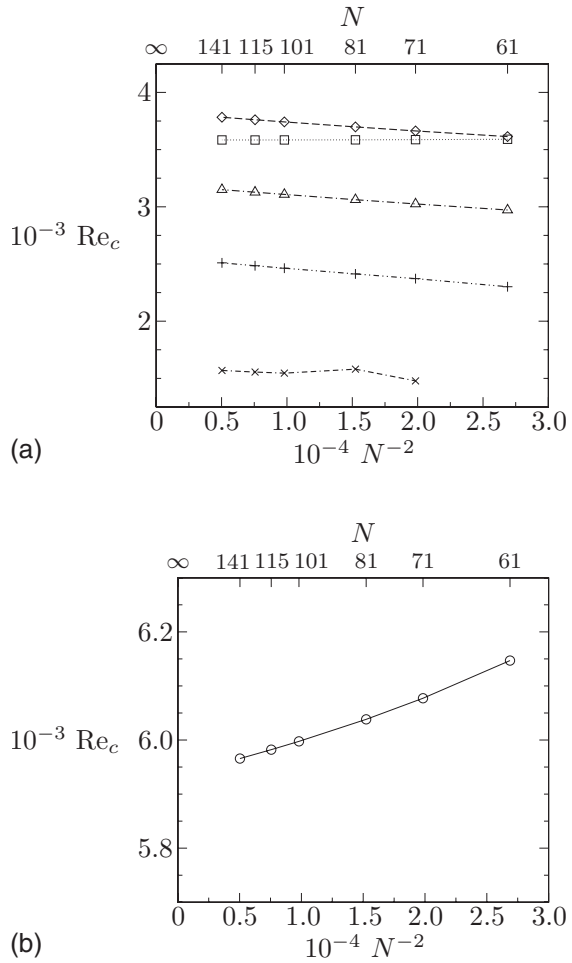


FIG. 2. Critical Reynolds numbers as functions of $N^{-2}$, where $N=N_x=N_y$. The symbols in (a) and (b) denote the aspect ratios $\Gamma=1.5$ (○), $\Gamma=2.1$ (□), $\Gamma=3$ (◇), $\Gamma=3.5$ (△), $\Gamma=4$ (+), and $\Gamma=6$ (×).

representative numerical linear-stability data in Table IV. There is a qualitative agreement of numerical and experimental results. In particular, the aspect ratio at which the character of the instability changes from steady to time dependent is about $\Gamma \approx 3$ for both kinds of approaches. However, there are differences. Most notably, the experimental critical Reynolds numbers are higher than the linear stability

TABLE III. Properties of the fluids used in the experiments of Refs. [3–6].

| Coefficient | Unit | Daviaud and Vince [3] | Sakurai *et al.* [4,5] | Burguete *et al.* [6] |
|---|---|---|---|---|
| $\beta$ | [1/K] | 0.00144 | 0.00135 | 0.00134 |
| $\gamma/\rho_0$ | [mm$^3$/s$^2$ K] | 110.6 | 118.0 | 105.3 |
| $\nu$ | [mm$^2$/s] | 0.65 | 0.65 | 0.65 |
| $d$ | [mm] | 10 | 10 | 10 |
| Pr | — | 10 | 9.8 | 10.3 |
| $\Gamma^2$ Bd | — | 12.755 | 11.220 | 12.488 |

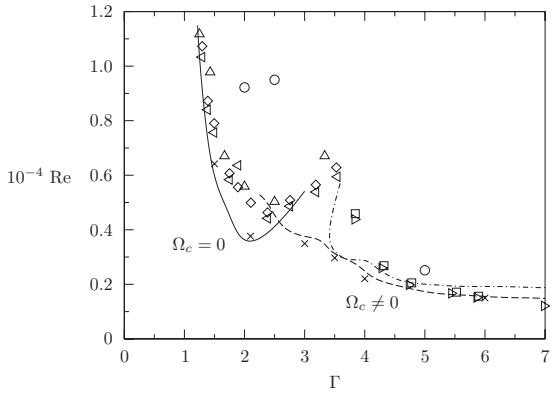


FIG. 3. Critical Reynolds number as a function of the aspect ratio Γ. The solid and the dashed lines indicate the critical curves for the steady and the oscillatory instability, respectively. The dashed-dotted line is the neutral curve for purely two-dimensional perturbations with $k=0$. Symbols indicate the experimental data of Ref. [3] (◇, □), Refs. [4,5] (△), and Ref. [6] (▷, ◁). The circles (○) are data of [5] indicating the onset of oscillations. Linear stability calculations with the slightly different values $\Gamma^2$ Bd=11.22 and Pr=9.8 corresponding to Refs. [4,5] are shown as crosses (×).

boundary. Apart from the possibility that the three-dimensional flow can only be observed when it has already reached a finite amplitude, the most likely explanation for this discrepancy is the heat-transfer condition at the free surface.

In the absence of any reliable information on the heat transfer at the free surface we have used adiabatic conditions. Even though the question of the heat transfer cannot be resolved by the present investigation, the good agreement for the critical wave numbers and the oscillation frequencies shown in Fig. 4 provides strong evidence that the linear stability analysis has indeed caught the essential physical behavior of the experiments. A further investigation of the instability mechanisms thus makes sense.

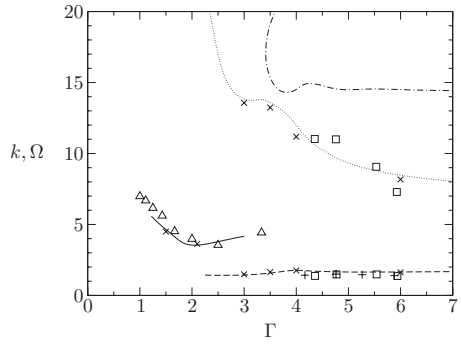


FIG. 4. Critical wave numbers (solid and dashed line) and frequencies (dotted and dashed-dotted line) as functions of Γ. The solid line indicates the three-dimensional steady mode $\Omega_c=0$. The dashed and the dotted lines denote the oscillatory mode. The dashed-dotted line indicates the frequency of the two-dimensional ($k=0$) oscillatory mode. Symbols denote the experimental data of Ref. [3] (□), Ref. [4] (△), and Ref. [65] (+). Additional numerical linear stability data for $\Gamma^2$ Bd=11.22 are indicated by ×.

TABLE IV. Representative linear stability data for Bond numbers and aspect ratios corresponding to the experimental conditions [3]. The numerical resolution was $141\times141$ grid points. The error is estimated by comparing the respective data with those obtained for a resolution of $71\times71$ grid points, except for $\Gamma=8$: For $\Gamma=8$ the critical data were computed on $221\times221$ grid points and the error deduced from a calculation with $141\times141$ grid points.

| $\Gamma$ | Bd | $\mathrm{Re}_c$ | $k_c$ | $\Omega_c$ |
|---|---|---|---|---|
| 1.50 | 5.669 | $5966\pm111$ | $4.645\pm0.020$ | 0 |
| 2.00 | 3.189 | $3633\pm8$ | $3.543\pm0.010$ | 0 |
| 2.50 | 2.041 | $4122\pm7$ | $3.788\pm0.010$ | 0 |
| 3.00 | 1.417 | $3783\pm120$ | $1.436\pm0.013$ | $13.86\pm0.12$ |
| 3.50 | 1.041 | $3150\pm125$ | $1.572\pm0.023$ | $13.61\pm0.17$ |
| 4.00 | 0.797 | $2510\pm138$ | $1.768\pm0.010$ | $12.04\pm0.23$ |
| 6.00 | 0.354 | $1569\pm91$ | $1.643\pm0.033$ | $8.46\pm0.05$ |
| 8.00 | 0.1993 | $1480\pm16$ | $1.663\pm0.006$ | $7.73\pm0.02$ |

### B. Mechanisms

For a detailed analysis of the steady and the oscillatory instabilities we consider the representative aspect ratios $\Gamma=2.1$, 4, and 8. In the framework of a linear stability analysis it is not possible to determine which of the two energy budgets, the mechanical or the thermal, is of greater importance to the instability mechanism. But the structures of the velocity and temperature fields in comparison with the spatial structures of the local energy-production terms can provide evidence for the relative importance of the two balances for the instability mode under consideration.

From Table V it is seen that the total energy production by buoyancy forces $\int_V BdV$ relative to the other mechanical production terms is very small or even negative (for $\Gamma=4$ and 8). Therefore, we can safely conclude that buoyancy is not a direct cause of the instabilities detected. Marangoni forces are important for all aspect ratios. This applies, in particular, to the span-wise Marangoni production $\int_S M_1 dS$. It shows that Marangoni forces drive a significant motion in the span-wise ($z$) direction, perpendicular to the plane of motion of the basic flow. We now have a closer look at the different aspect ratios.

TABLE V. Energy terms integrated over one period of the critical mode for several aspect ratios $\Gamma$.

| Aspect ratio | $\Gamma=2.10$ | $\Gamma=4.00$ | $\Gamma=8.00$ |
|---|---|---|---|
| $\mathrm{Re}_c$ | 3584.4 | 2510.2 | 1463.9 |
| Bd | 2.8923 | 0.7972 | 0.1993 |
| $\int_V I_1 dV$ | 0.034 | 0.024 | −0.010 |
| $\int_V I_2 dV$ | 0.594 | 0.217 | 0.071 |
| $\int_V I_3 dV$ | −0.071 | 0.000 | 0.000 |
| $\int_V I_4 dV$ | 0.022 | 0.010 | 0.004 |
| $\int_S M_1 dS$ | 0.236 | 0.541 | 0.617 |
| $\int_S M_2 dS$ | 0.042 | 0.222 | 0.333 |
| $\int_V BdV$ | 0.146 | −0.011 | −0.015 |
| $\int_V J_1 dV$ | 0.991 | 0.754 | 0.351 |
| $\int_V J_2 dV$ | 0.017 | 0.250 | 0.659 |

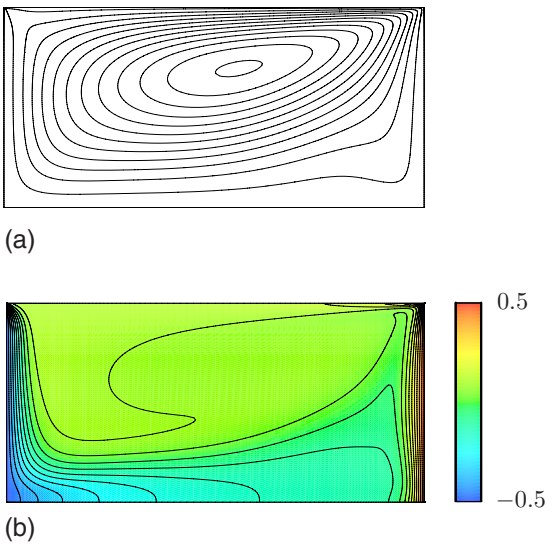


FIG. 5. (Color online) Basic state streamlines (a) and temperatures field (b) for $\Gamma=2.1$ at the critical Reynolds number $\mathrm{Re}=\mathrm{Re}_c=3584.4$ and $k_c=3.544$.

#### 1. Stationary instability for $\Gamma=2.1$

In order to discuss the instability mechanism we must keep in mind the main features of the basic state which is shown in Fig. 5. The basic velocity field is characterized by a single vortex which is strained elliptically. The basic temperature field exhibits a nearly isothermal region in the vortex core and thermal boundary layers near the cold and hot walls. The Marangoni number $\mathrm{Ma}=\mathrm{Re}\,\mathrm{Pr}$ is sufficiently high such that cold fluid is transported from the cold wall along the insulating bottom of the cavity very close up to the hot corner where it forms a *cold finger*. By a similar convective transport a *warm finger* is created in front of the thermal boundary layer on the cold wall.

For the aspect ratio $\Gamma=2.1$, which corresponds to the minimum of the critical curve $\mathrm{Re}_c(\Gamma)$, the two mechanisms associated with $I_2$ and $J_1$ are potentially important (Table V). Both production terms take their maximum value in identical periodic planes $z=$const. Let us first consider the thermal production rate $J_1$. This term describes the amplification of the temperature perturbation by horizontal convection in $x$ direction due to the perturbation flow. The perturbation flow is shown as arrows in Fig. 6 in a plane $z=$const in which $J_1$ as well as $I_2$ take their maxima. In the plane shown the perturbation flow is mainly directed toward the cold wall (negative $x$ direction), but it also has a small component in negative $y$ direction. The component of the perturbation flow which is perpendicular to the basic-state isotherms gives rise to a perturbation temperature field [Fig. 6(a)]. Associated with this convective effect is the thermal-energy production rate $J_1$ [Fig. 6(b)] which is sharply peaked near the (left) cold wall where the perturbation flow impinges on the thermal boundary layer. The production rate $J_2$ which is associated

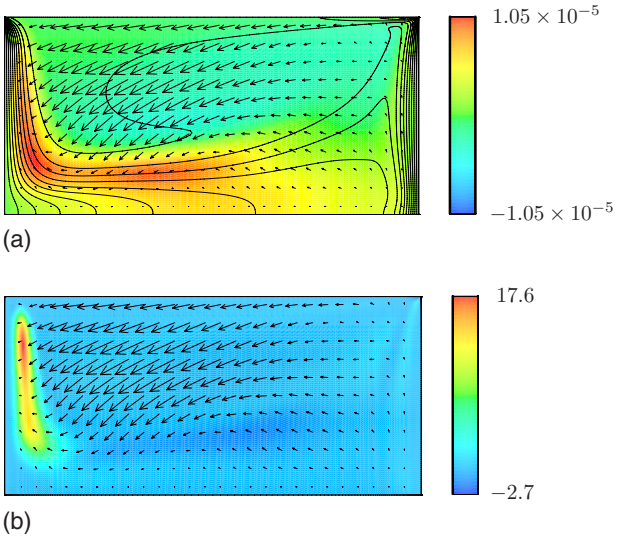


FIG. 6. (Color online) Critical perturbation flow field (arrows) for $\Gamma=2.1$ in the common plane $z=$const in which both $I_1$ and $J_2$ take their maximum value. In addition, (a) shows the basic-state isotherms (lines) and the critical perturbation temperature (color) and (b) displays the thermal energy production $J_1$ (color).

with the the vertical convection is not shown. As can be seen from Figs. 6(a) and 7 the strong perturbation-temperature maximum on the cold wall is advected by the basic flow along the bottom of the cavity and up along the hot wall where it reaches the free surface. One of the resulting small hot free-surface spots is visible on the right-hand side of Fig. 7. However, owing to their small size, they do not appear to drive a significant perturbation flow.

Considering the $x$-component $u$ of the free surface flow, we notice that the perturbation velocity $u$ on the free surface in the colder half of the cavity (left-hand side of Fig. 7) is in opposition to the Marangoni stresses resulting from the perturbation-temperature field, i.e., the perturbation surface flow is directed away from the large cold surface spot. Thus, the perturbation velocity $u$ in $x$ direction cannot be caused by the Marangoni effect which is associated with the large free-surface temperature-perturbation spots. This result is consistent with the observation of Braunsfurth and Homsy [40] of a *nonintuitive* reverse flow against the temperature gradient (of the total flow) in their experiments for supercritical Reynolds numbers.

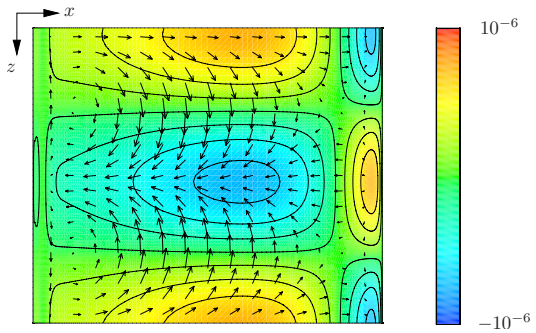


FIG. 7. (Color online) Surface temperature (color) and perturbation velocity field (arrows) at the free surface $y=0.5$.

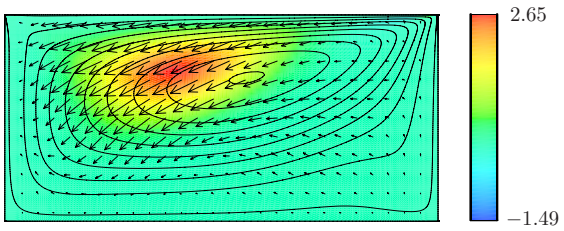


FIG. 8. (Color online) Kinetic energy production $I_2$ (color) and perturbation velocity (arrows) together with the basic-state streamlines in a plane $z=$const in which $I_2$ takes its maximum.

We now turn to the mechanical energy budget. The major fraction of about 60% of the kinetic-energy production is contributed by $I_2$. This term describes the amplification of the horizontal perturbation flow $u$ by the vertical advection of horizontal momentum ($u_0$) of the basic state. Since $I_2$ is peaked in the region of the maximum perturbation velocity (Fig. 8), the perturbation flow gains most of its energy from the strong basic shear flow near the free surface, triggered by the vertical component of the perturbation flow midway between the heated walls. This process leads to regions of very high absolute values of the horizontal (streamwise) perturbation velocity which are called streaks. While a streak ($x$ component of $\mathbf{u}$) in negative $x$ direction is created by the downward $y$ component of $\mathbf{u}$ (Fig. 6), a streak in positive $x$ direction is created by the upward $y$ component of $\mathbf{u}$ in an $(x,y)$ plane shifted by half a wavelength. The positive and negative streaks are connected by a turning flow in $z$ direction. At midplane ($y=0$) the turning flow is visible in Fig. 9. The opposite return flow in $z$ direction occurs near the free surface and is not visible in the plane $y=0$, but on the free surface in Fig. 7.

The same mechanism of amplification of the perturbation energy is operative in wall-bounded plane shear flows [54], where the process of streak formation is called *lift up*. It is a linear process which leads to an algebraic transient growth of the perturbation energy [55]. While the linear perturbations ultimately decay in unbounded parallel shear flows, they persist through an exponential instability in the present thermocapillary-flow system. This qualitative difference is due to the finite aspect ratio and aiding Marangoni forces which close the instability loop.

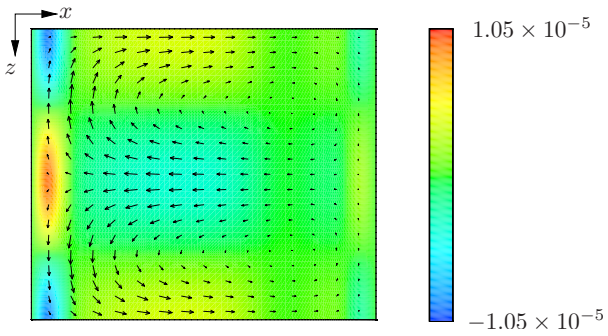


FIG. 9. (Color online) Perturbation flow (arrows) and perturbation temperature field (color) at the horizontal midplane of the cavity $y=0$.

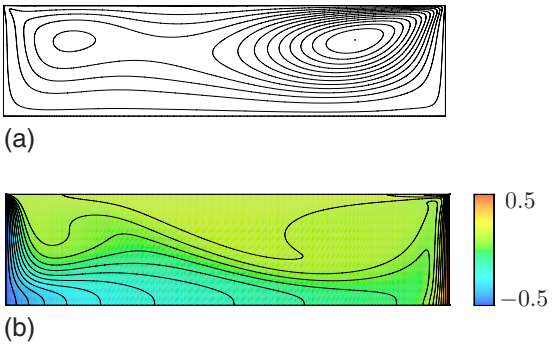


FIG. 10. (Color online) Basic state for $\Gamma=4$. Lines and colors denote the streamlines and the temperature field, respectively.

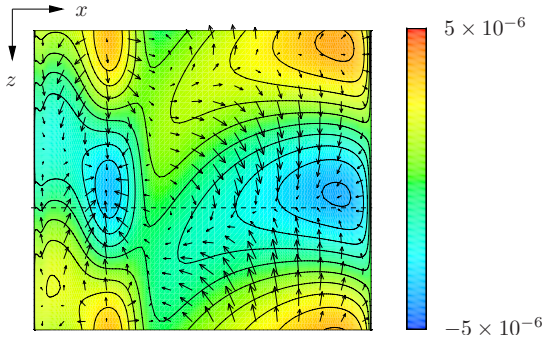


FIG. 11. (Color online) Perturbation flow (arrows) and temperature-perturbation field (color and lines) on the free surface for $\Gamma=4$ and $\mathrm{Re}=2510.2$. The wave propagates in negative $z$ direction (to the top in the figure). The dashed line indicates the plane shown in Fig. 12.

The streaks generated by the lift-up process act on the basic temperature field and create relatively weak internal temperature perturbations. In the plane shown in Fig. 6(a) the perturbation flow creates a weak cold perturbation-temperature spot in the interior by transporting cold fluid from the cold finger to the center of the cavity. This process also occurs near the free surface and gives rise to the large cold free-surface spot visible in Fig. 7. An analogous mechanism creates the large hot free-surface spots by convection from the hot finger. The Marangoni effect in $z$ direction due to the large but weak free-surface spots assists the mechanical instability by creating the required vertical perturbation flow due to continuity in the region of strong shear.

The direct production rate of mechanical energy by the span-wise Marangoni effect, represented by $\int_S M_1 \mathrm{d}S$, contributes only by roughly one quarter to the total kinetic-energy production (Table V). This is different from the hydrothermal-wave mechanism in high-Prandtl-number thermocapillary liquid bridges in which the Marangoni effect is practically responsible for the total mechanical energy production (see Fig. 16 of Ref. [56]).

We conclude that the stationary instability branch for $\Gamma \lesssim 3$ and $\mathrm{Pr}=10$ is due to a combined inertial and thermocapillary effect. The major cause (60% of the kinetic energy production) of the instability is provided by the lift-up process taking place in the shear flow below the free surface and creating streaks in $\pm x$ direction. In fact, the Reynolds number defined as $\mathrm{Re}_{u_0} := \max(|\mathbf{u}_0|)h/\nu$ is $\approx 200$ at criticality for the stationary instability, underlining the importance of inertia. The basic temperature field is mainly necessary to provide the driving of the basic shear flow. The presence of the hot and cold fingers in the basic temperature field provide an additional mechanism (25% of the kinetic energy production) in support of the mechanical instability mechanism by enabling span-wise thermocapillary forces which result from a stream-wise advection of the basic temperature due to the streaks.

### 2. *Oscillatory instability for* $\Gamma=4$

The basic state for $\Gamma=4$ is shown in Fig. 10. The flow consist of a strong eddy attached to the hot right-hand-side wall. Its counterclockwise circulation drags hot fluid from the hot-wall boundary layer along the free surface and toward the cold wall. Embedded in the return flow is a small region of closed streamlines near the cold wall. Apart from the thermal layer on the hot wall and the somewhat thicker layer on the cold wall there exists also a sizable temperature gradient in the vicinity of the hyperbolic stagnation point which is formed by the strong eddy near the hot wall and the weaker, embedded eddy near the cold wall.

The energy budgets (Table V) show that the perturbation flow is primarily driven by Marangoni forces with a total of approximately 76%. The dominating mechanical energy production term is $M_1$ which amounts to 54%. It arises due to Marangoni stresses in $z$ direction. An additional driving of the perturbation flow, albeit much weaker, is caused by the process $I_2$ which builds on the horizontal shear $\partial u_0/\partial y$. The importance of $M_1$ relative to $I_2$ is reversed here as compared to aspect ratio $\Gamma=2.1$. Therefore, the present oscillatory instability is primarily due to thermocapillary effects.

The critical mode arises in the form of a pair of waves traveling in $\pm z$ direction. We discuss the mechanism by considering the temperature and flow perturbations of the critical wave traveling in negative $z$ direction. The temperature perturbation on the free surface is shown in Fig. 11. Within one wavelength in $z$ direction four surface-temperature extrema arise. The two major temperature spots are located near the hot right-hand-side wall. Since Marangoni forces dominate the kinetic energy budget, we can safely assume that the four surface-temperature extrema per period drive the perturbation-flow field. Both cold surface spots arise near the plane $z=\mathrm{const}$ in which $I_2$ takes its maximum value (dashed line in Fig. 11). This plane is shown in Fig. 12. One can identify two streams from the free surface which arise below

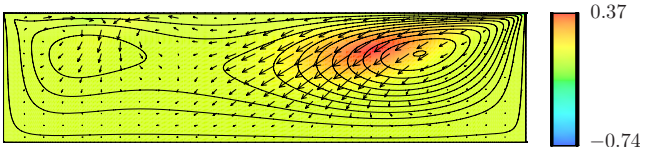


FIG. 12. (Color online) Kinetic energy production $I_2$ (color) in the plane in which $I_2$ takes its maximum value (dashed line in Fig. 11). This plane is close to the one at which the surface-temperature perturbation has a minimum. Also shown are the basic streamlines and the perturbation velocity field (arrows).

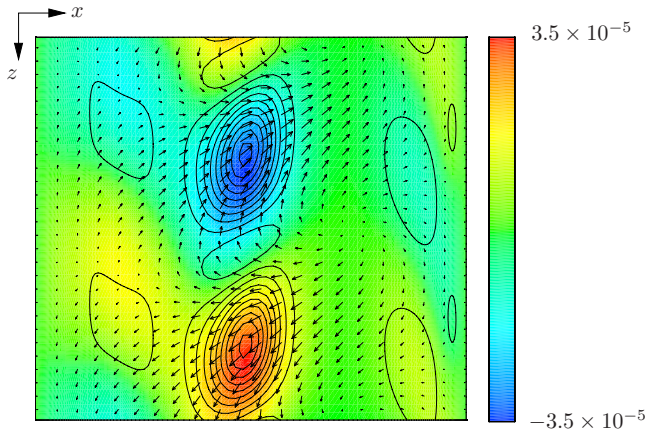


FIG. 13. (Color online) Temperature perturbation (color), thermal production (isolines), and perturbation velocity vectors in a horizontal cut at $y=-0.1$ through the global extrema of the perturbation temperature field. The window is the same as in Fig. 11.

the two cold spots due to continuity. From this figure we see that the perturbation flow $v$ down from the major cold surface spot is associated with a component $u$ in such a way that the stream can extract some additional kinetic energy from the basic flow. The associated contribution $I_2$ is shown in color (online) in Fig. 12. This process is similar as for $\Gamma=2.1$. The cold free-surface spot near the cold wall is much weaker and the corresponding downward stream cannot extract any significant kinetic energy from the basic velocity field, because the stream is weak and the basic flow does not exhibit strong shear in the colder (left) half of the cavity.

As both cold surface spots originate in approximately the plane $z=$const a head-on collision in the same plane of the respective downward streams would result in smaller-scale perturbation-flow structures which would be damped. In fact, the opposing streams escape a collision by turning in opposing $z$ directions near the midplane (Fig. 13). The two antiparallel oblique streams are directed toward the hyperbolic stagnation point of the basic flow where they meet the basic-state isotherms in an oblique way. As a result, strong internal temperature extrema are created (Fig. 13) as the streams transport warm fluid from the warm (right) side of the cavity into the cold (left) side of the cavity and vice versa. The associated production rate $J_1$ by horizontal convection is shown in Fig. 14 in a plane in which it takes its maximum. It can be seen from Fig. 13 that the major production-rate extrema of $J_1$ (lines) are slightly offset in negative $z$ direction from the internal temperature extrema (color). Like the absence of any mirror symmetry at constant $z$ this is a characteristic sign of a wave traveling in negative $z$ direction.

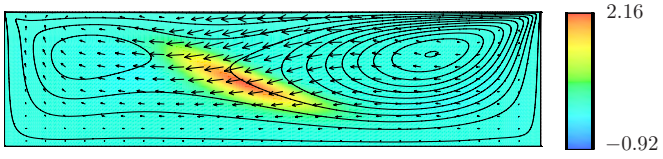


FIG. 14. (Color online) Thermal energy production $J_1$ (color) in a plane $z=$const in which $J_1$ takes its maximum value. Lines and vectors indicate the basic-flow streamlines and the perturbation-velocity field, respectively.

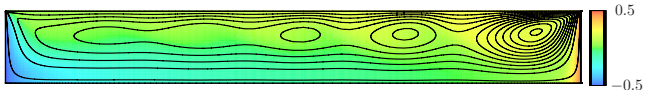


FIG. 15. (Color online) Basic state for $\Gamma=8$ and $\mathrm{Re}=\mathrm{Re}_c=1463.9$. Lines and color indicate the streamlines and the temperature field, respectively.

Owing to the relatively large Prandtl number the hot and cold spots generated near the hyperbolic stagnation point (line) are advectively transported by the basic flow away from the stagnation point in two opposing directions: directly toward the free surface near the cold corner region and, in the opposite direction, along the bottom of the cavity toward the hot corner region. The major surface spots are then created by conduction over a relatively small distance. This mechanism is very similar to the hydrothermal wave mechanism in high-Prandtl-number fluid layers [13]. However, since the advective transport $\mathbf{u}_0\cdot\nabla\theta$ is of crucial importance, the particular form of the hydrothermal wave differs from the plane waves in the return flow of an infinite layer [12].

### 3. Oscillatory instability for $\Gamma=8$

The two-dimensional steady basic state for $\Gamma=8$ is shown in Fig. 15 at the critical Reynolds number $\mathrm{Re}_c=1463.9$ (grid $141\times141$). The critical wave number and frequency are given in Table IV. The streamline pattern shows the well-known structure of a sequence of corotating eddies embedded in a global return flow [16–18,30,32,57]. According to Priede and Gerbeth [16] and Riley and Neitzel [17] the first instability in plane layers arises in the form of steady corotating vortices if $\mathrm{Bd}>0.22$. Only for $\mathrm{Bd}<0.22$ the first instability in infinite layers is due to hydrothermal waves. The present condition $\mathrm{Bd}=0.20$, corresponding to the parameters of Ref. [3], is slightly lower than the codimension-two point and indicates that hydrothermal waves should be favored. Accordingly, the strong perturbation of the ideal return-flow solution caused by the rigid hot wall gives rise to corotating rolls whose amplitude decays with the distance from the hot wall. Apart from the boundary layers on the heated walls the temperature field is essentially stratified from cold near the bottom to hot at the free surface. However, horizontal variations of $\theta_0$ exist which are characterized by a mean gradient superposed by spatial oscillations reflecting the embedded two-dimensional vortices.

From Table V we see that more than 90% of the kinetic energy production is caused by the thermocapillary driving forces. Hence, inertia effects are not important in the instability mechanism. The perturbation flow is just acting as a link in the chain to sustain the temperature-perturbation field. The temperature perturbation is fed by the convective action of the perturbation-velocity field on the basic temperature field. Both thermal production terms $J_1$ and $J_2$ are important, the latter term representing the major contribution. The total local thermal production rate $J=J_1+J_2$ is shown in Fig. 16 as an isosurface (gray) for $J=0.07$. By comparing the intersection of the isosurface with the streamlines of the basic flow

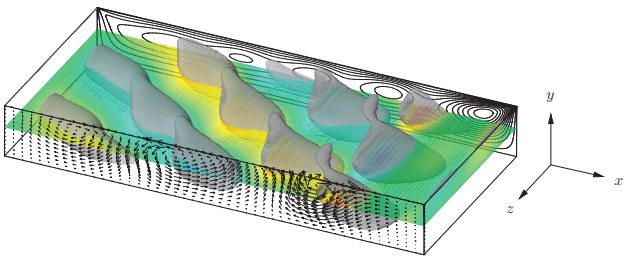


FIG. 16. (Color) Perturbation temperature in the plane $y=0.07$ (color) and isosurface (gray) of the total local thermal energy production $J=J_1+J_2$ at $J=0.07$. The background shows the basic streamlines and the foreground displays the perturbation velocity field in that plane $z=$const.

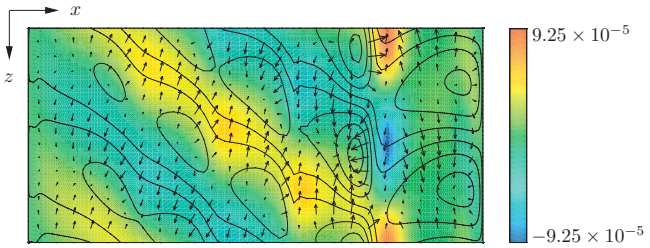


FIG. 17. (Color) Surface-temperature (isolines) and surface velocity (arrows) in comparison to the internal temperature field at $y=0.07$ (color).

(background of Fig. 16) it can be seen that the thermal production is peaked in the regions of the hyperbolic stagnation points of the basic flow where relatively large basic temperature variations exist (Fig. 15). In these regions the perturbation flow is relatively strong (foreground of Fig. 16), which explains the structure of the thermal production. The local maxima of the production rate are well pronounced near the hot wall, whereas the production rate becomes smoother toward the cold wall and the isolated isosurfaces shown merge into a oblique varicose tube. The perturbation temperature field is also shown in Fig. 16 in the plane $y=0.07$ in which the absolute maximum occurs. The temperature perturbation extrema lag behind the thermal production rate extrema indicating that the wave propagates obliquely toward the hot wall and in negative $z$ direction. The angle of propagation with respect to the temperature gradient is $\alpha_c \approx 50°$.

In the same way as described for $\Gamma=4$ above, the internal perturbation temperature extrema are transported by the basic flow to the free surface where they appear as weak hot and cold spots. These are shown as isolines in Fig. 17. The surface-temperature extrema (lines) lag behind the corresponding temperature extrema in the bulk (color). Even though the surface-temperature extrema near the hot wall are not as well aligned as the strong internal perturbation temperature extrema, the alignment becomes better away from the hot wall and a plane-hydrothermal-wave structure seems to emerge. All the features found are qualitatively the same as for hydrothermal waves in the return flow [12,13]. Merely, the wave is strongly affected here by the underlying basic flow structure. In particular, the processes in the hot near-wall region, which are essentially the same as for $\Gamma=4$, contribute substantially to the instability.

## IV. DISCUSSION AND CONCLUSION

### A. Stationary instability

The stationary instability found for $\Gamma=2.1$ is consistent with the previous nonlinear simulations of Mundrane and Zebib [37]. A detailed analysis of the energy-production terms reveals that the instability mechanism can be traced back to a process which is mainly mechanical. According to our analysis, the stationary instability is characterized by streaks in the shear layer of the free surface which are triggered by a small vertical component of the perturbation velocity. By horizontal advection of temperature from the hot and cold fingers of the basic state the streaks produce free-surface-temperature extrema which drive a span-wise Marangoni flow supporting the streak formation. The thermal energy budget is insignificant, because the thermal energy created by the convective action of the streaks on the cold-wall thermal boundary layer is essentially dissipated and the convection of thermal energy by the basic flow merely leads to weak and small surface temperature perturbations near the hot wall. It is obvious that this mechanical mechanism is at work also for similar aspect ratios along the neutral curve of the stationary mode.

The similarity of the present stationary instability in the thermocapillary system with the stationary instability in the two-sided lid-driven cavity with antiparallel wall motion, which is purely mechanical, is noteworthy. In the driven cavity a similar basic flow in the form of a strained vortex is created (for $\Gamma=1.5$, e.g., see Fig. 9 of Ref. [50]). In both systems the predominant mechanism of amplification is identical and the critical modes arise in the form of cellular vortices (see also [58]). The return flow from the streaks in the lid-driven cavity is solely due to continuity and the finite size of the cavity. In the thermocapillary cavity the same mechanism holds, but it is assisted by mild Marangoni forces. The key feature of the basic flow in both cases is the straining of the basic vortex into an elliptic one. Since both instabilities share many properties with the instability of dipolarly strained, unbounded vortices [59], they appear to be closely related to the elliptic instability [60,61]. A similar mechanism, besides centrifugal effects, is also operative in low-Prandtl-number thermocapillary half-zones [62].

For infinite layers Mercier and Normand [19] found that a sufficient buoyancy level is required for the onset of stationary rolls. They speculated, moreover, that the thermal boundary conditions of a conducting bottom wall and a heat transfer at the free surface were decisive for a comparison with the experimental results of Ref. [3], even though it was not possible to simultaneously fit the values of the Biot and Bond numbers to the experimental ones. The present work has shown, however, that the experimental results can be well reproduced if one assumes insulating top (zero Biot number) and bottom boundary conditions. Moreover, the mechanism that we find is independent of gravity. This latter result is qualitatively different from the results in plane layers in which stationary instabilities are usually associated with Prandtl numbers larger than 1 and a vertical temperature

profile which is at least piecewise destabilizing in the sense of the Marangoni [12,63] or the Rayleigh-Bénard instability [64]. The buoyancy-driven instability in form of stream-wise rolls found by Mercier and Normand [19] in plane layers must thus have a different cause.

### B. Oscillatory instabilities

The oscillatory instabilities for aspect ratio $\Gamma=4$ and $\Gamma=8$ are dominated by Marangoni effects. They turn out to be more efficient in producing kinetic energy than the inertial coupling terms. Qualitatively, the mechanisms are the same as for hydrothermal waves in the return flow of plane thermocapillary layers. However, the particular structure of the waves is strongly influenced by the underlying nonparallel basic flow. This applies, in particular, to small aspect ratios (e.g., to $\Gamma=4$). The results for $\Gamma=8$ demonstrate how plane hydrothermal waves may emerge in the limit $\Gamma\to\infty$. Nevertheless, the hydrothermal-wave structure remains strongly affected by the basic return flow in a region of at least $\Delta x\approx 2$ from the hot wall.

The direction of propagation of the hydrothermal wave sufficiently far from the side walls is quite sensitive to the parameters. For the present insulating boundary conditions we find an angle with respect to the temperature gradient of $\alpha_c\approx 50°$. This angle of wave propagation is smaller than the value $\alpha\approx 80°$ observed by Daviaud and Vince [3]. On the other hand, it is much larger than the critical angle $\alpha^{\mathrm{layer}}(\mathrm{Pr}=10)=21.4°$ for a hydrothermal wave at $\mathrm{Bd}=0$ in an infinite thermocapillary layer [2,12]. For the slightly larger Prandtl number of $\mathrm{Pr}=13.9$ and for $\mathrm{Bd}=0.2$ Priede and Gerbeth [16] confirmed the angle of 22° for plane layers even in the presence of gravity, in agreement with the experimental result of Riley and Neitzel [17]. By a three-dimensional numerical simulation in a large-aspect-ratio cavity for $\mathrm{Pr}=13.9$ and zero gravity, Xu and Zebib [27] found an angle of propagation of ≈15°, which is even less than the value for plane thermocapillary layers $\alpha_c^{\mathrm{layer}}(\mathrm{Pr}=13.9)\approx 17$. It must be taken into account, however, that the value of 15° was obtained for a nonlinear solution in the form of a wave traveling in stream-wise and standing in span-wise direction. On the other hand, our result for $\mathrm{Pr}=10$ is in good agreement with the result $\alpha_c=46.6°$ of Mercier and Normand [19] for infinite thermocapillary-buoyant layers with a slight heat loss characterized by a Biot number of $\mathrm{Bi}=1$. The experimental result of Burguete *et al.* [6] for $\mathrm{Pr}=10.3$, aspect ratio $\Gamma=9.1$ ($h=1.1$ mm, $L_x=10$ mm), and a similar Bond number $\mathrm{Bd}=0.15$ is $\alpha\approx 30°$, which is also significantly higher than the pure thermocapillary case. Pelacho, Garcimartín, and Burguete [35] pointed out that the rather different angle of propagation of $\alpha\approx 80°$ found by Ref. [3] in comparison to their own experimental result may have been influenced by the three-dimensional geometry of the cavity. For a stream-wise length of $L_x=100$ mm, a layer depth of 1.5 mm, and $\mathrm{Pr}=10$, Ref. [35] found that the angle of propagation of the wave is slightly larger than $\alpha=50°$ for a span-wise length of $L_y=40$ mm and that $\alpha$ decays to about 40° when increasing $L_y$ to $L_y=100$ mm.

We thus conclude that the angle of propagation is sensitive both to the geometrical constraints and the thermal boundary conditions. The dependence on the aspect ratio might be related to the fact that, once the wave number $k_c$ in $z$ direction is given, the angle which the emerging structure of the critical flow makes with the temperature gradient cannot align freely, because it is restricted by the periodicity in $z$ and the structure of the basic flow which is roughly periodic in $x$ direction due to the embedded corotating vortices. The underlying basic-flow structure is important in so far as it determines the location of the energy production extrema near the hyperbolic stagnation points. As can be seen from Fig. 16 the present critical mode for $\Gamma=8$ provides a grid of $4\times 2$ production extrema due to the four hyperbolic points in $x$ direction and the double periodicity of $J$ in $z$ direction. In fact, the wave number of the corresponding plane hydrothermal wave $k^{\mathrm{HW}}=k_c/\sin\alpha\approx 2.2$ which does not deviate much from the theoretical value $k_c^{\mathrm{layer}}\approx 2.53$ for plane layers.

### C. Conclusions

We have studied in detail the flow instabilities in thermocapillary-buoyant cavities of $\mathrm{Pr}=10$ for adiabatic top and bottom boundary conditions and for periodic boundary conditions in the span-wise direction. The free surface was assumed to be undeformable ($\mathrm{Ca}\to 0$) and the Bond number was selected according to the experimental conditions of Refs. [3,5,6]. For representative aspect ratios we have analyzed the instability mechanisms by evaluating the various integrals of the Reynolds-Orr equation and their integrands. While similar results can be expected for slightly different parameters, other instabilities may arise upon large parameter variations. For instance, centrifugal instabilities are dominating for small Prandtl numbers [24].

Similar stationary and oscillatory instabilities have been predicted numerically for annular systems containing fluids of moderately large Prandtl numbers. Peng *et al.* [48] argued that the stationary instability detected in deep thermocapillary annular pools of $\mathrm{Pr}=6.7$ with $\Gamma<4$ is due to buoyancy, because the local Rayleigh number exceeds the critical value of $\mathrm{Ra}_c=657$ for no-slip boundary conditions in layers heated from below. In their simulations the inverted temperature gradient arises due to a turning back of the cold finger near the hot wall. We have shown, however, that common to all steady and oscillatory instabilities found here, the production of kinetic energy by buoyancy is very weak. For that reason buoyancy as a major direct factor for the instability can be ruled out. On the other hand, buoyancy may be of importance indirectly, as it influences the basic flow and temperature fields. Since no stationary instabilities have been found by Sim, Zebib, and Schwabe [44] in their simulations for a cylindrical configuration under zero gravity, we conclude that it is the change of the basic velocity field due to buoyancy which enables the stationary instability, not the inverted basic temperature gradient.

## ACKNOWLEDGMENTS

We gratefully acknowledge computing time provided by ZARM of the University of Bremen and by ZID of the Vienna University of Technology.

[1] *Handbook of Crystal Growth*, edited by D. T. J. Hurle (North Holland, Amsterdam, 1994).
[2] H. C. Kuhlmann, *Thermocapillary Convection in Models of Crystal Growth*, Springer Tracts in Modern Physics No. 152 (Springer, Berlin, 1999).
[3] F. Daviaud and J. M. Vince, Phys. Rev. E **48**, 4432 (1993).
[4] M. Sakurai, H. C. Kuhlmann, and H. J. Rath, Z. Angew. Math. Mech. **80**, 701 (2000).
[5] M. Sakurai, H. C. Kuhlmann, and H. J. Rath, Z. Angew. Math. Mech. **81**, 953 (2001).
[6] J. Burguete, N. Mukolobwiez, F. Daviaud, N. Garnier, and A. Chiffaudel, Phys. Fluids **13**, 2773 (2001).
[7] A. Zebib, G. M. Homsy, and E. Meiburg, Phys. Fluids **28**, 3467 (1985).
[8] B. M. Carpenter and G. M. Homsy, Phys. Fluids A **2**, 137 (1990).
[9] B. M. Carpenter and G. M. Homsy, J. Fluid Mech. **207**, 121 (1989).
[10] A. K. Sen and S. H. Davis, J. Fluid Mech. **121**, 163 (1982).
[11] R. V. Birikh, J. Appl. Mech. Tech. Phys. **7**, 43 (1966).
[12] M. K. Smith and S. H. Davis, J. Fluid Mech. **132**, 119 (1983).
[13] M. K. Smith, Phys. Fluids **29**, 3182 (1986).
[14] P. Laure, B. Roux, and H. Ben Hadid, Phys. Fluids A **2**, 516 (1990).
[15] J.-F. Mercier and C. Normand, Int. J. Heat Mass Transfer **45**, 793 (2002).
[16] J. Priede and G. Gerbeth, Phys. Rev. E **56**, 4187 (1997).
[17] R. J. Riley and G. P. Neitzel, J. Fluid Mech. **359**, 143 (1998).
[18] D. Villers and J. K. Platten, J. Fluid Mech. **234**, 487 (1992).
[19] J. F. Mercier and C. Normand, Phys. Fluids **8**, 1433 (1996).
[20] H. Ben Hadid and B. Roux, J. Fluid Mech. **221**, 77 (1990).
[21] M. Ohnishi, H. Azuma, and T. Doi, Acta Astronaut. **26**, 685 (1992).
[22] H. Ben Hadid and B. Roux, J. Fluid Mech. **235**, 1 (1992).
[23] M. Mundrane and A. Zebib, Phys. Fluids **6**, 3294 (1994).
[24] F. Schimmel, S. Albensoeder, and H. Kuhlmann, Proc. Appl. Math. Mech. **5**, 583 (2005).
[25] S. Albensoeder, H. C. Kuhlmann, and H. J. Rath, Phys. Fluids **13**, 121 (2001).
[26] L. J. Peltier and S. Biringen, J. Fluid Mech. **257**, 339 (1993).
[27] J. Xu and A. Zebib, J. Fluid Mech. **364**, 187 (1998).
[28] E. Bucchignani and D. Mansutti, Phys. Rev. E **69**, 056319 (2004).
[29] E. Bucchignani, Phys. Fluids **16**, 3839 (2004).
[30] V. M. Shevtsova and J. C. Legros, Acta Astronaut. **52**, 541 (2003).
[31] V. M. Shevtsova, A. A. Nepomnyashchy, and J. C. Legros, Phys. Rev. E **67**, 066308 (2003).
[32] C. D. Saedeleer, A. Garcimartin, G. Chavepeyer, J. K. Platten, and G. Lebon, Phys. Fluids **8**, 670 (1996).
[33] D. Schwabe, U. Möller, J. Schneider, and A. Scharmann, Phys. Fluids A **4**, 2368 (1992).
[34] A. B. Ezersky, A. Garcimartín, H. L. Mancini, and C. Pérez-García, Phys. Rev. E **48**, 4414 (1993).
[35] M. A. Pelacho, A. Garcimartín, and J. Burguete, Phys. Rev. E **62**, 477 (2000).
[36] P. Gillon and G. M. Homsy, Phys. Fluids **8**, 2953 (1996).
[37] M. Mundrane and A. Zebib, Phys. Fluids A **5**, 810 (1993).
[38] M. A. Pelacho and J. Burguete, Phys. Rev. E **59**, 835 (1999).
[39] S. Benz and D. Schwabe, Exp. Fluids **31**, 409 (2001).
[40] M. G. Braunsfurth and G. M. Homsy, Phys. Fluids **9**, 1277 (1997).
[41] N. Garnier and A. Chiffaudel, Eur. Phys. J. B **19**, 87 (2001).
[42] S. Hoyas, H. Herrero, and A. M. Mancho, Phys. Rev. E **66**, 057301 (2002).
[43] D. Schwabe, A. Zebib, and B.-C. Sim, J. Fluid Mech. **491**, 239 (2003).
[44] B.-C. Sim, A. Zebib, and D. Schwabe, J. Fluid Mech. **491**, 259 (2003).
[45] Y.-R. Li, L. Peng, Y. Akiyama, and N. Imaishi, J. Comput. Phys. **259**, 374 (2003).
[46] S. Hoyas, A. M. Mancha, H. Herrero, N. Garnier, and A. Chiffaudel, Phys. Fluids **17**, 054104 (2005).
[47] W. Shi and N. Imaishi, J. Cryst. Growth **290**, 280 (2006).
[48] L. Peng, Y.-R. Li, W.-Y. Shi, and N. Imaishi, Int. J. Heat Mass Transfer **50**, 872 (2007).
[49] W. H. Press, B. P. Flannery, S. A. Teukolsky, and W. T. Vetterling, *Numerical Recipes (FORTRAN)* (Cambridge University Press, Cambridge, 1989).
[50] S. Albensoeder and H. C. Kuhlmann, J. Fluid Mech. **458**, 153 (2002).
[51] S. Albensoeder, H. C. Kuhlmann, and H. J. Rath, Theor. Comput. Fluid Dyn. **14**, 223 (2001).
[52] S. Albensoeder and H. C. Kuhlmann, Eur. J. Mech. B/Fluids **21**, 307 (2002).
[53] R. A. W. M. Henkes and P. Le Quéré, J. Fluid Mech. **319**, 281 (1996).
[54] J. Hamilton, J. Kim, and F. Waleffe, J. Fluid Mech. **287**, 317 (1995).
[55] M. T. Landahl, J. Fluid Mech. **98**, 243 (1980).
[56] M. Wanschura, V. S. Shevtsova, H. C. Kuhlmann, and H. J. Rath, Phys. Fluids **7**, 912 (1995).
[57] M. F. Schatz and G. P. Neitzel, Annu. Rev. Fluid Mech. **33**, 93 (2001).
[58] H. C. Kuhlmann, M. Wanschura, and H. J. Rath, J. Fluid Mech. **336**, 267 (1997).
[59] C. Eloy and S. Le Dizès, Phys. Fluids **13**, 660 (2001).
[60] R. T. Pierrehumbert, Phys. Rev. Lett. **57**, 2157 (1986).
[61] B. J. Bayly, Phys. Rev. Lett. **57**, 2160 (1986).
[62] C. Nienhüser and H. C. Kuhlmann, J. Fluid Mech. **458**, 35 (2002).
[63] J. R. A. Pearson, J. Fluid Mech. **4**, 489 (1958).
[64] G. Z. Gershuni, P. Laure, V. M. Myznikov, and E. M. Zhukhovitsky, Microgravity Q. **2**, 141 (1992).
[65] M. Sakurai (private communication).